The U2H map explains the effect of (sub)mesoscale turbulence on significant wave height statistics

HAN WANG[1] , ANA B. VILLAS BÔAS[2] , JACQUES VANNESTE[3] AND WILLIAM R. YOUNG[4]

[1] *Institut für Meereskunde, Universität Hamburg, Hamburg 20146, Germany,* [2] *Department of Geophysics, Colorado School of Mines, Golden CO 80401, USA,* [3] *School of Mathematics and Maxwell Institute for Mathematical Sciences, University of Edinburgh, Edinburgh EH9 3FD, UK,* [4] *Scripps Institution of Oceanography, University of California at San Diego, La Jolla CA 92093-0213, USA*

ABSTRACT: Currents modulate the energy of surface gravity waves, leading to spatial inhomogeneities in significant wave height (SWH). Previous work indicates that the overall scale of the inhomogeneities is set by the scale of the currents, that the inhomogeneities are strongly anisotropic even for isotropic currents, and that the rotational and divergent components of the currents have sharply distinct effects. We explain these and other features of current-induced SWH inhomogeneities using the U2H map, a linear relation between SWH and currents deduced from wave-action conservation by making simplifying assumptions. We obtain a linear law relating the spectrum of SWH to the spectra of rotational and divergent kinetic energy of the current. This makes it possible to relate SWH statistics (such as variance and anisotropy) to the current statistics and wave properties including directional spreading.

1. Introduction

Ocean surface gravity waves (SGWs) are primarily driven by wind but are influenced by ocean currents, which modify their direction, frequency, and amplitude (Phillips 1977; Cavaleri et al. 2012). In recent years, recognition of the role of meso- and submesoscale turbulence in modulating SGWs has grown, driven by advances in numerical modeling (e.g., Rascle et al. 2014; Ardhuin et al. 2017; Romero et al. 2020; Villas Bôas et al. 2020) and remote sensing observations (e.g., Rascle et al. 2016; Romero et al. 2017; Quilfen and Chapron 2019; Lenain and Pizzo 2021). While currents affect all moments of the SGW spectrum, recent studies have particularly focused on their influence on significant wave height (SWH), which is routinely observed by satellite altimeters and widely used in air–sea flux parametrizations (e.g., Taylor and Yelland 2001; Edson et al. 2013). Collectively, findings from this series of recent studies on wave–current interactions suggest the following:

(i) rotational currents induce larger SWH anomalies than do divergent currents;

(ii) the spatial scales of the SWH anomaly are determined by those of the current, i.e. similar spectral slopes;

(iii) the SWH response to divergent currents is local (largest where the current is strongest) but the response to rotational currents is non-local and anisotropic.

Despite progress in our understanding of the relationship between currents and SWH anomalies, the exact mechanisms leading to points (i)–(iii) remain unclear.

Figure 1 shows the SWH anomaly, denoted $h_s(x, y)$, induced by synthetic random currents. The mean kinetic energy of the currents is fixed, while the slope of the kinetic energy spectrum and the ratio between the rotational and divergent energy of the current are varied. Features (i), (ii) and (iii) are evident: the magnitude of h_s decreases as the proportion of rotational currents decreases, the spatial scales of h_s are larger when the spatial scale of the current is larger, and the patterns of h_s are stretched in the primary wave direction (chosen as the positive x-direction) when currents are rotational.

The main difference between figure 1 and figure 4 of Villas Bôas et al. (2020) is the way in which SWH anomalies are computed: here we obtain h_s using the U2H map developed in Wang et al. (2025, hereafter W25), while in Villas Bôas et al. (2020) h_s is obtained by running WAVEWATCH III (WAVE height, WATer depth and Current Hindcasting, Tolman et al. 2009 – hereafter we refer to this model as WW3). U2H is a linear map giving the SWH anomalies directly as a function of the current without resorting to solving the full wave-action conservation equation. In W25, we compare the U2H map against WW3 in a few current configurations and establish a good match between the two methods.

While Villas Bôas et al. (2020) focus their attention on highly directional wave spectra, here we do not. We examine how the directionality of the wave spectrum affects features (i), (ii) and (iii). This is illustrated in figure 2 which is similar to figure 1 but for a wave spectrum with broad angular spread. For this broad spectrum, features (i) and (ii) continue to hold, though less evidently for (i), but feature (iii) does not. Comparing figures 1 and 2 – and noting the difference in the color maps – shows that:

(iv) the SWH anomaly h_s is larger for highly directional background waves.

Here we take advantage of the simple, explicit form of U2H to explain and quantify features (i)–(iv). We also clarify the relation between current and SWH spectra, refining our understanding of feature (iii), particularly where rotational and divergent currents have different spatial scales.

2. U2H map: the recipe

The W25 recipe for the U2H map has two ingredients:

- the SGW action spectrum in the absence of currents, hereafter referred to as the background spectrum, $\bar{\mathcal{A}}(\boldsymbol{k})$, assumed independent of time and space;

- the surface current velocity $\boldsymbol{U}(\boldsymbol{x})$, assumed independent of time and with spatial scales much larger than SGW wavelengths.

The background significant wave height associated with $\bar{\mathcal{A}}(\boldsymbol{k})$ is

$$\bar{H}_s = \left(\frac{16}{g} \int \bar{\mathcal{A}}(\boldsymbol{k}) \sigma(k) \, \mathrm{d}\boldsymbol{k} \right)^{1/2}, \tag{1}$$

where g is the gravitational acceleration, $k = |\boldsymbol{k}|$, and

$$\sigma(k) = \sqrt{gk} \tag{2}$$

is the intrinsic frequency of deep-water SGWs. $\bar{H}_s$ is constant in space.

The current $\boldsymbol{U}(\boldsymbol{x})$ modulates the SGWs, leading to a spatially dependent SWH

$$H_s(\boldsymbol{x}) = \bar{H}_s + h_s(\boldsymbol{x}), \tag{3}$$

where $h_s(\boldsymbol{x})$ is the current-induced SWH anomaly. The U2H map assumes that the typical current speed U is small compared to the group speed c_g of the waves:

$$U/c_g \ll 1. \tag{4}$$

U2H then provides an approximation to the relative SWH anomaly $h_s(\boldsymbol{x})/\bar{H}_s$ at order $O(U/c_g)$.

The map is best formulated using the Helmholtz decomposition of the current into purely divergent and purely rotational parts,

$$\boldsymbol{U}(\boldsymbol{x}) = \nabla \phi(\boldsymbol{x}) + \nabla^{\perp} \psi(\boldsymbol{x}), \tag{5}$$

where ϕ and ψ are the velocity potential and streamfunction. We introduce the Fourier transform

$$\hat{\boldsymbol{U}}(\boldsymbol{q}) = \int \boldsymbol{U}(\boldsymbol{x}) \mathrm{e}^{-\mathrm{i}\boldsymbol{q}\cdot\boldsymbol{x}} \, \mathrm{d}\boldsymbol{x} \tag{6}$$

of the current velocity, with $\boldsymbol{q}$ the Fourier vector (not to be confused with the SGW wavevector $\boldsymbol{k}$). Eq. (5) becomes

$$\begin{aligned} \hat{\boldsymbol{U}}(\boldsymbol{q}) &= \mathrm{i}\boldsymbol{q}\hat{\phi}(\boldsymbol{q}) + \mathrm{i}\boldsymbol{q}^{\perp}\hat{\psi}(\boldsymbol{q}) \\ &= \hat{U}_{\phi}(\boldsymbol{q})\boldsymbol{e}_{\boldsymbol{q}} + \hat{U}_{\psi}(\boldsymbol{q})\boldsymbol{e}_{\boldsymbol{q}}^{\perp}, \end{aligned} \tag{7}$$

where $q = |\boldsymbol{q}|$, $\boldsymbol{q}^{\perp}$ is obtained from $\boldsymbol{q}$ by rotation by $\pi/2$ about a vertical axis, and $\boldsymbol{e}_{\boldsymbol{q}} = \boldsymbol{q}/q$ and $\boldsymbol{e}_{\boldsymbol{q}}^{\perp} = \boldsymbol{q}^{\perp}/q$ are unit vectors. In terms of the polar representation $\boldsymbol{q} = q(\cos\varphi, \sin\varphi)$, $\boldsymbol{q}^{\perp} = q(-\sin\varphi, \cos\varphi)$. The U2H map expressed in Fourier space is then

$$\frac{\hat{h}_s(\boldsymbol{q})}{\bar{H}_s} = \hat{L}_{\phi}(\varphi)\widehat{U}_{\phi}(\boldsymbol{q}) + \hat{L}_{\psi}(\varphi)\widehat{U}_{\psi}(\boldsymbol{q}). \tag{8}$$

$\hat{L}_{\phi}(\varphi)$ and $\hat{L}_{\psi}(\varphi)$ are determined by the background action spectrum and control the impact of the divergent and rotational parts of the current on h_s. (These functions are denoted as $\hat{L}_{\parallel}(\varphi)$ and $\hat{L}_{\perp}(\varphi)$ in W25, respectively.) A crucial result is that $\hat{L}_{\phi}(\varphi)$ and $\hat{L}_{\psi}(\varphi)$ depend on the Fourier vector $\boldsymbol{q}$ only through the polar angle φ. They are given by

$$\hat{L}_{\phi}(\varphi) = -\frac{32}{g\bar{H}_s^2} \boldsymbol{P} \cdot \boldsymbol{e}_{\boldsymbol{q}}, \tag{9}$$

and

$$\hat{L}_{\psi}(\varphi) = \frac{16}{g\bar{H}_s^2} \left(\sum_{n=-\infty}^{\infty} n(-\mathrm{i})^{|n|} 2\pi p_n \mathrm{e}^{n\mathrm{i}\varphi} - 2\boldsymbol{P} \cdot \boldsymbol{e}_{\boldsymbol{q}}^{\perp} \right), \tag{10}$$

where

$$2\pi p_n \stackrel{\text{def}}{=} \int_0^{2\pi} \mathrm{e}^{-\mathrm{i}n\theta} \int_0^{\infty} \bar{\mathcal{A}}(k,\theta) k^2 \mathrm{d}k \, \mathrm{d}\theta. \tag{11}$$

The wave momentum $\boldsymbol{P}$ in (9) and (10) is

$$\boldsymbol{P} = \begin{pmatrix} +\mathrm{Re}\, 2\pi p_1 \\ -\mathrm{Im}\, 2\pi p_1 \end{pmatrix}. \tag{12}$$

Equations (8)–(12) include all the formulas required to compute the U2H map from the background action spectrum $\bar{\mathcal{A}}(k,\theta)$ and current velocity $\boldsymbol{U}(\boldsymbol{x})$. These formulas are linear in $\boldsymbol{U}(\boldsymbol{x})$ and $\bar{\mathcal{A}}(k,\theta)$, and require minimal computational resources. The computational implementation is straightforward, as described and illustrated with a Jupyter notebook in W25. In addition to the assumptions already mentioned, the U2H map neglects forcing, dissipation and wave–wave interactions.

In examples shown here, we follow W25 and assume that the background spectrum takes a separable form

$$\bar{\mathcal{A}}(k,\theta) = f(k)D(\theta). \tag{13}$$

We take $f(k)$ to be a truncated Gaussian distribution in intrinsic frequency concentrated around a peak value σ_m
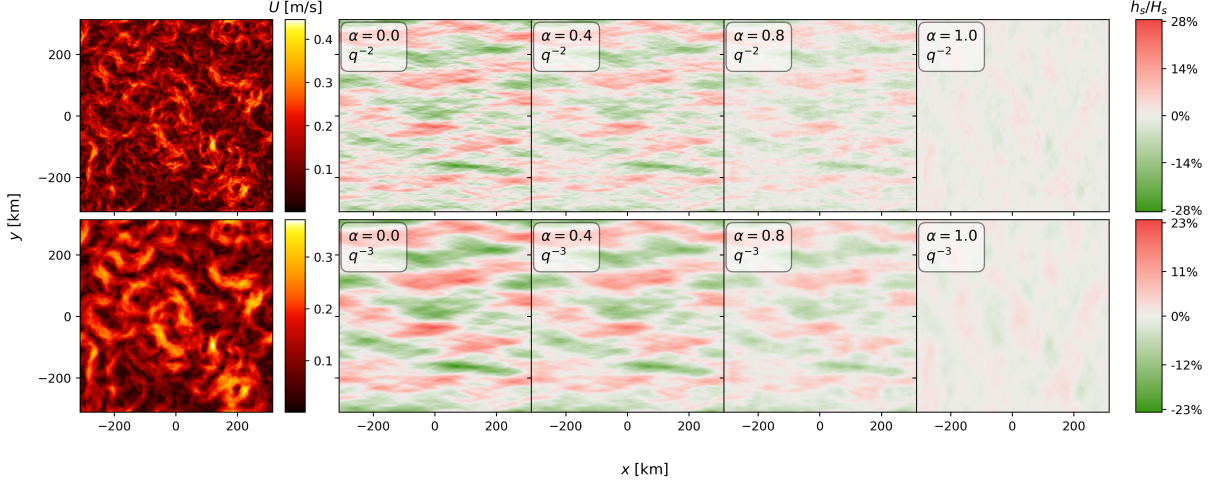
FIG. 1: Impact of currents on SWH anomaly h_s. The current speed, $\sqrt{u^2 + v^2}$, is shown in the first column. The KE spectrum of the current is isotropic and the isotropic spectra follow the power laws q^{-2} (top row) and q^{-3} (bottom row), where q is the wavenumber. The relative SWH anomaly $h_s/\bar{H}_s$ is shown for four values of the parameter α defined in (32) controlling the ratio of rotational to divergent current kinetic energy (columns two through five, with purely rotational current in column two and purely divergent current in column five). The waves have a wave action spectrum with directional-width parameter $s = 40$ in (14) and the primary wave direction is along the x-axis. See section 4 for details.
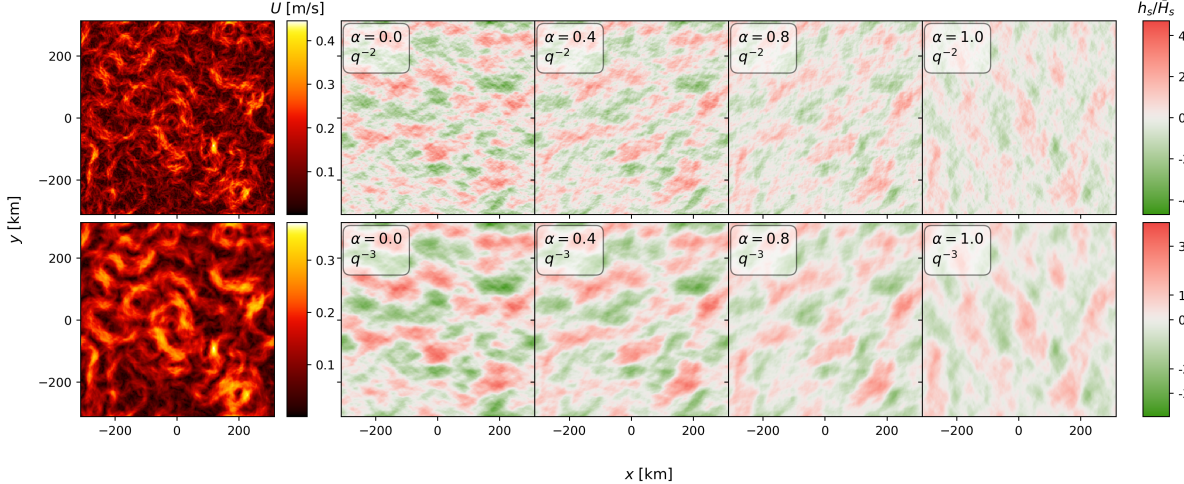

FIG. 2: Same as figure 1 but with directional-width parameter $s = 1$ in (14) corresponding to a less directional spectrum. Note the difference in color scale compared with figure 1.

(see appendix A for details). We set $\sigma_m = 2\pi/10.3 \text{ s}^{-1}$ for all the results of the paper except in section 7 which considers the sensitivity to σ_m.

The angular dependence $D(\theta)$ follows the model of Longuet-Higgins et al. (1963, hereafter LHCS):

$$D(\theta) \propto \cos^{2s}\left((\theta - \theta_p)/2\right), \qquad (14)$$

where θ_p is the primary angle of wave propagation taken as 0, and s is the directional-width parameter, with large s corresponding to a small directional spreading.

We emphasize that the U2H map can be employed with arbitrary background spectra, including non-separable ones, and that our qualitative conclusions do not depend on our specific choice of the LHCS model spectrum. For highly directional spectra, in particular, the LHCS param-
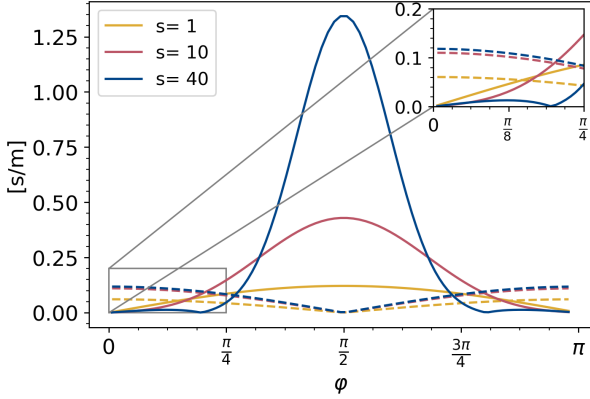
FIG. 3: $|\hat{L}_\phi|$ (dashed lines) and $|\hat{L}_\psi|$ (solid lines) computed from (11)–(12) for the LHCS spectrum (14) with $\theta_p = 0$ and for the directional-width parameter $s = 1$, 10 and 40. A zoomed-in view for $0 \leq \varphi < \pi/4$ is shown at the upper right corner.

eter s can be interpreted more generally as $s = 2/\delta^2$, where $\delta \ll 1$ is the directional spreading (e.g. Kuik et al. 1988).

Figure 3 shows $|\hat{L}_\phi|$ and $|\hat{L}_\psi|$ for three values of s. Because h_s and U are real,

$$\hat{L}_\phi(-\varphi) = -\hat{L}_\phi^*(\varphi) \quad \text{and} \quad \hat{L}_\psi(-\varphi) = -\hat{L}_\psi^*(\varphi). \quad (15)$$

In figure 3 we exploit this symmetry to restrict the range of φ to $0 < \varphi < \pi$. For highly directional spectra, i.e. $s \gg 1$, $|\hat{L}_\psi|$ is localised around a maximum at $\varphi = \pi/2$ and is much larger than $|\hat{L}_\phi|$. Asymptotic results reported in W25 explain these features by showing that $\hat{L}_\psi(\varphi)$ is localised in $O(s^{-1/2})$ regions around $\varphi = \pm\pi/2$ where it scales like s. In contrast, $\hat{L}_\phi(\varphi)$ is $O(1)$ and s-independent for $s \gg 1$.

3. Power spectral relations

W25 validate the U2H map (8) by comparing its predictions to WW3 simulations for a few specific current configurations. In this paper we focus on the relationship between the statistics of SWH and the statistics of U implied by (8). We assume that $U(x)$ is a homogeneous random field and define the spectra and cross-spectrum of the divergent and rotational parts of the current as

$$\hat{C}^{U_\phi}(\boldsymbol{q}) \stackrel{\text{def}}{=} \langle|\hat{U}_\phi(\boldsymbol{q})|^2\rangle = q^2\langle|\hat{\phi}(\boldsymbol{q})|^2\rangle, \quad (16)$$

$$\hat{C}^{U_\psi}(\boldsymbol{q}) \stackrel{\text{def}}{=} \langle|\hat{U}_\psi(\boldsymbol{q})|^2\rangle = q^2\langle|\hat{\psi}(\boldsymbol{q})|^2\rangle, \quad (17)$$

and

$$\hat{C}^{U_\phi U_\psi}(\boldsymbol{q}) \stackrel{\text{def}}{=} \langle\hat{U}_\phi^*(\boldsymbol{q})\hat{U}_\psi(\boldsymbol{q})\rangle = q^2\langle\hat{\phi}^*(\boldsymbol{q})\hat{\psi}(\boldsymbol{q})\rangle, \quad (18)$$

where $\langle\cdot\rangle$ denotes ensemble average.

From (8) the SWH spectrum, defined as the power spectrum

$$\hat{C}^{h_s}(\boldsymbol{q}) = \langle|\hat{h}_s(\boldsymbol{q})/\bar{H}_s|^2\rangle \quad (19)$$

of the relative change in SWH, is given by

$$\hat{C}^{h_s}(\boldsymbol{q}) = |\hat{L}_\phi(\varphi)|^2\hat{C}^{U_\phi}(\boldsymbol{q}) + |\hat{L}_\psi(\varphi)|^2\hat{C}^{U_\psi}(\boldsymbol{q})$$
$$+ 2\,\text{Re}\left(\hat{L}_\phi^*(\varphi)\hat{L}_\psi(\varphi)\hat{C}^{U_\phi U_\psi}(\boldsymbol{q})\right), \quad (20)$$

where Re denotes the real part. Eq. (20) is central to this paper. It provides a simple relationship between the SWH spectrum and the spectra characterising the currents.

We assume for simplicity that the currents are isotropic, with uncorrelated divergent and rotational parts. This reduces (20) to

$$\hat{C}^{h_s}(\boldsymbol{q}) = \frac{1}{\pi q}\left(|\hat{L}_\phi(\varphi)|^2 K_\phi(q) + |\hat{L}_\psi(\varphi)|^2 K_\psi(q)\right), \quad (21)$$

where $K_\phi(q)$ and $K_\psi(q)$ are the current divergent and rotational kinetic energy isotropic spectra, with e.g.

$$K_\phi(q) = \frac{1}{2}\int \hat{C}^{U_\phi}(\boldsymbol{q})q\,\mathrm{d}\varphi = \pi q\hat{C}^{U_\phi}(\boldsymbol{q}). \quad (22)$$

The assumption of uncorrelatedness $\hat{C}^{U_\phi U_\psi} = 0$ is not essential for many of our results, as discussed in appendix B.

While $\hat{C}^{h_s}(\boldsymbol{q})$ is not isotropic because of the angular dependence of $\hat{L}_\phi(\varphi)$ and $\hat{L}_\psi(\varphi)$, we can define the SWH isotropic spectrum

$$\hat{C}^{h_s}(q) \stackrel{\text{def}}{=} \int \hat{C}^{h_s}(\boldsymbol{q})q\,\mathrm{d}\varphi, \quad (23)$$

where we abuse notation in marking the difference between isotropic and two-dimensional spectra only by displaying the different independent variable, q vs. $\boldsymbol{q}$. Integrating (21) over φ leads to

$$\hat{C}^{h_s}(q) = 2\left(\ell_\phi K_\phi(q) + \ell_\psi K_\psi(q)\right) \quad (24)$$

where the coefficients ℓ_ϕ and ℓ_ψ are

$$(\ell_\phi, \ell_\psi) = \frac{1}{2\pi}\int \left(|\hat{L}_\phi(\varphi)|^2, |\hat{L}_\psi(\varphi)|^2\right)\mathrm{d}\varphi. \quad (25)$$

We examine the consequences of (24) in the next two sections before considering the anisotropy of $\hat{C}^{h_s}(\boldsymbol{q})$ in section 6.

4. Variance

We first study the variance of the SWH anomaly. Variance reflects the overall intensity of the anomaly, and helps understand features (i) and (iv) observed in section 1.
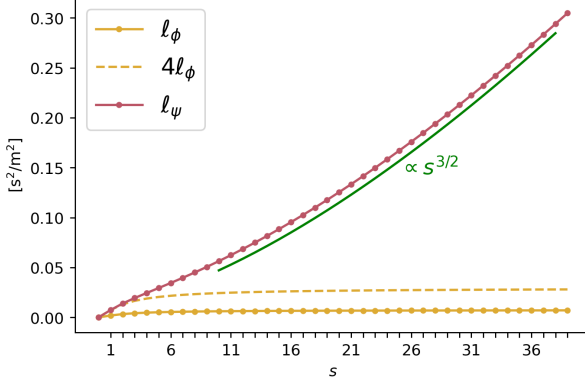
FIG. 4: ℓ_ψ and ℓ_ϕ as functions of s, assuming the LHCS angular dependence. The green curve indicates the $s^{3/2}$ dependence of ℓ_ψ that holds when $s \gg 1$.

Integrating (24) with respect to q and recalling from Parseval's identity that the variance of a homogeneous random field is the integral of its spectrum, we obtain a relation between the variance of the SWH and the variances of the divergent and rotational current speeds:

$$\langle h_s^2/\bar{H}_s^2 \rangle = \ell_\phi \langle |U_\phi|^2 \rangle + \ell_\psi \langle |U_\psi|^2 \rangle. \qquad (26)$$

Similarly, multiplying (24) by q^2 and integrating gives

$$\langle |\nabla h_s|^2/\bar{H}_s^2 \rangle = \ell_\phi \langle D^2 \rangle + \ell_\psi \langle Z^2 \rangle, \qquad (27)$$

where D and Z denote surface divergence and vorticity.

Thus, the variance of SWH is a weighted sum of the variances of the speed of the divergent and rotational parts of the current. And the variance of the gradient of SWH is the weighed sum of the variances of the divergence and vorticity of the current. In both cases, the weights are ℓ_ϕ and ℓ_ψ in (25).

Figure 4 shows ℓ_ψ and ℓ_ϕ for the LHCS model spectrum (14) as functions of s. For $s = 1$, $\ell_\psi = 4\ell_\phi$. As s increases, corresponding to more directional wave spectra, ℓ_ψ increases, as $s^{3/2}$ for $s \gg 1$ (this can be established from the large-s form of $\hat{L}_\psi$ mentioned at the end of section 2), while ℓ_ϕ saturates at a much smaller value. These properties of ℓ_ψ and ℓ_ϕ explain features (i) and (iv) noted in section 1, i.e. the dominance of rotational currents over divergent currents, and the increase in the magnitude of SWH anomalies with wave directionality.

To quantity these effects, we express ℓ_ϕ and ℓ_ψ in terms of p_n in (11) by substituting (9) and (10) into (25) to find

$$\ell_\phi = \frac{1}{4}\left(\frac{32}{g\bar{H}_s^2}\right)^2 |\boldsymbol{P}|^2 \qquad (28)$$

$$\ell_\psi = \left(\frac{32}{g\bar{H}_s^2}\right)^2 |\boldsymbol{P}|^2 + \frac{1}{2}\left(\frac{32}{g\bar{H}_s^2}\right)^2 \sum_{|n|\geq 2} n^2 |p_n|^2. \qquad (29)$$

Combining the two equations above

$$\ell_\psi = 4\ell_\phi + \frac{1}{2}\left(\frac{32}{g\bar{H}_s^2}\right)^2 \sum_{|n|\geq 2} n^2 |p_n|^2, \qquad (30)$$

and therefore, as observed in Figure 4,

$$\ell_\psi \geq 4\ell_\phi. \qquad (31)$$

The large-s behaviour of ℓ_ϕ and ℓ_ψ can be explained by the corresponding asymptotic form of $\hat{L}_\phi(\varphi)$ and $\hat{L}_\psi(\varphi)$ (see W25).

We illustrate (26) in Figure 5. This shows the SWH variance $\langle |h_s|^2/\bar{H}_s^2 \rangle$ computed for an ensemble of synthetic, randomly drawn currents. For all currents, the isotropic kinetic energy spectra $K_\phi(q)$ and $K_\psi(q)$ have the same shape, corresponding to a power law q^γ over a finite range of q with isotropic spectral slope $\gamma = -1, -2$ and -3 (see Appendix C for details). The magnitudes of K_ϕ and K_ψ are varied in such a way that the total kinetic energy $K = K_\phi + K_\psi$ is a constant (0.01 m²/s² per kilogram). Figure 5 shows $\langle |h_s|^2/\bar{H}_s^2 \rangle$ as a function of the parameter $0 \leq \alpha \leq 1$ such that

$$K_\phi(q) = \alpha K(q) \quad \text{and} \quad K_\psi(q) = (1-\alpha)K(q), \qquad (32)$$

and for three values of s. As expected from (26), the SWH variance $\langle |h_s|^2/\bar{H}_s^2 \rangle$ is independent of the spectral slope γ, linear in α, and increasing with s (since combining (26) with (32) shows the SWH variance is proportional to $\alpha\ell_\phi + (1-\alpha)\ell_\psi$). We have checked that the SWH gradient variance behaves as indicated by (27).

5. Isotropic spectrum

We now examine the implications of formula (24) for the SWH isotropic spectrum $\hat{C}^{h_s}(q)$. According to (24), $\hat{C}^{h_s}(q)$ is the weighted sum of the divergent and rotational kinetic energy spectra $K_\phi(q)$ and $K_\psi(q)$, with q-independent weights ℓ_ϕ and ℓ_ψ. This explains feature (ii) of section 1: the length scales of h_s are set by those of the current.

When the divergent and rotational spectra share an identical spectral slope, as in Villas Bôas et al. (2020) and in figures 1 and 2, it follows from (24) that $\hat{C}^{h_s}(q)$ has
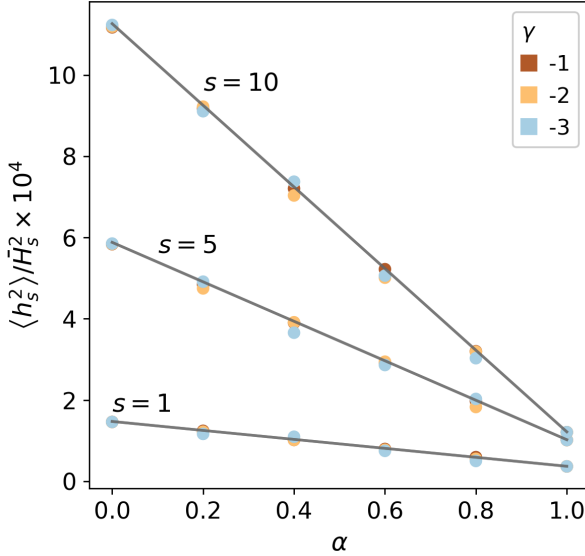
FIG. 5: Variance $\langle h_s^2 \rangle / \bar{H}_s^2$ of the SWH anomaly as a function of the parameter α controlling the ratio of divergent to rotational kinetic energy of the current. Three values of the spectral slope $\gamma = -1, -2$ and -3 are considered. Estimates from random samples (dots) are compared with the prediction (26) (lines).

the same spectral slope. In typical oceanic flows, however, the rotational spectrum $K_\psi(q)$ is steep, dominating the total KE at large scales, and the divergent spectrum K_ϕ is shallower, dominating the total KE at small scales (Bühler et al. 2014; Rocha et al. 2016; Balwada et al. 2016; Chereskin et al. 2019). For such flows (24) predicts that $\hat{C}^{h_s}(q)$ is parallel to $K_\psi(q)$ at large scales and to $K_\phi(q)$ at small scales. Because $\ell_\psi > 4\ell_\phi$, the transition scales between steep and shallow spectra arises at smaller scales for $\hat{C}^{h_s}(q)$ than for $K(q)$. The shift towards small scales is particularly pronounced for waves with high directionality ($s \gg 1$) for which $\ell_\psi \gg \ell_\phi$.

In Figure 6 we compare the SWH spectrum $\hat{C}^{h_s}(q)$ to the divergent, rotational and total energy spectra of the currents for $s = 1$ (left panel) and $s = 10$ (right panel). The energy spectra $K_\phi(q)$ and $K_\psi(q)$ are taken as the power laws q^{-1} and q^{-3}, respectively, with amplitudes such that the wavenumber where $K_\psi(q) = K_\phi(q)$ is $q = 2\pi/(100 \text{ km})$. (These parameters are chosen for pedagogical purpose and are not intended to agree with realistic currents.) The background wave spectrum is as in section 4. The spectrum $\hat{C}^{h_s}(q)$ is obtained by computing $h_s(\boldsymbol{x})/\bar{H}_s$ for 10 random current realizations using the U2H map and averaging. This spectrum is as expected, making a transition from steep to shallow at a scale smaller than the transition in the total energy spectrum. In the strongly directional case $s = 10$, the transition is shifted to such a small scale that

$\hat{C}^{h_s}(q)$ is parallel to the energy spectrum only at large scales. This is reminiscent of results reported in Ardhuin et al. (2017), where the agreement between the spectral slopes of $\hat{C}^{h_s}(q)$ and $K(q)$ is noted only at large scales.

For currents such as those of Figure 6, dominated by rotation at large scales and by divergence at small scales, the form of $\hat{C}^{h_s}(q)$ implies that the overall scale of the SWH anomaly h_s is larger than the scale of the current, markedly so for highly directional waves. This is confirmed by Figure 7 which shows h_s in physical space for a single realization of the currents with the same parameters as for Figure 6. The anisotropy of h_s is striking and demands quantification.

6. Anisotropy

We first examine the anisotropy of the SWH anomaly by contrasting the one-dimensional spectra

$$\hat{C}^{h_s}(q_1) = \frac{1}{2\pi} \int \hat{C}^{h_s}(q_1, q_2) \, dq_2 \tag{33}$$

and

$$\hat{C}^{h_s}(q_2) = \frac{1}{2\pi} \int \hat{C}^{h_s}(q_1, q_2) \, dq_1 \tag{34}$$

corresponding to observations of h_s along or across the primary wave direction.

Figure 8 shows these spectra together with analogous KE spectra for the current and wave parameters of Figure 6 and for $s = 1$ and 10. In the along-wave direction, $\hat{C}^{h_s}(q_1)$ peaks at the lowest wavenumbers regardless of the spectral slope of the KE spectra. The slope of $\hat{C}^{h_s}(q_1)$ for small q_1 increases with s, corresponding to increasingly large scales dominating the along-wave SWH signal.

In the across-wave direction, $\hat{C}^{h_s}(q_2)$ peaks at scales close to the KE peak, but has a spectral slope closer to the rotational KE (steeper than the total KE for realistic oceanic currents) and thus leading to SWH scales larger than the current scales. These properties of $\hat{C}^{h_s}(q_1)$ and $\hat{C}^{h_s}(q_2)$ reflect the streaky nature of the SWH anomaly seen in Figures 1, 2 and 7. They can be fully understood by combining the closed-form expression (33)–(34) with the explicit expression (21) for $\hat{C}^{h_s}(\boldsymbol{q})$ and the form of $\hat{L}_\phi(\varphi)$ and $\hat{L}_\psi(\varphi)$ shown in Figure 4. In the limit of large s, the asymptotic behaviors seen in Figure 3 (discussed in section 2) amplify these properties, leading to more streaky SWH anomalies.

A simple measure of the anisotropy of h_s is the aspect ratio λ_x/λ_y of typical lengthscales in the along- and across-wave directions. This ratio can be defined by

$$\left(\frac{\lambda_x}{\lambda_y}\right)^2 = \frac{\langle(\partial_y h_s)^2\rangle}{\langle(\partial_x h_s)^2\rangle} = \frac{\iint q_2^2 \hat{C}^{h_s}(\boldsymbol{q}) \, d\boldsymbol{q}}{\iint q_1^2 \hat{C}^{h_s}(\boldsymbol{q}) \, d\boldsymbol{q}}, \tag{35}$$
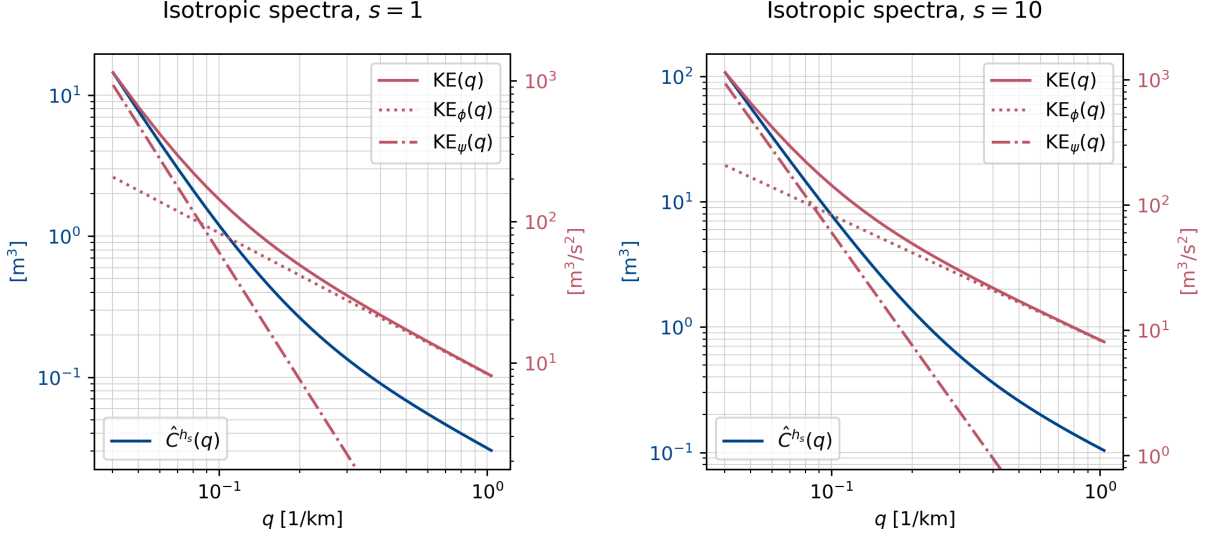
FIG. 6: Isotropic spectrum $\hat{C}^{h_s}(q)$ and KE spectra (total, divergent and rotational KE) for the examples in section 5. The wave directional-width parameter s is 1 (left panel) and 10 (right panel). The left vertical axis is for $\hat{C}^{h_s}(q)$ and the right vertical axis is for the KE spectra. Spectra outside $(200\text{km}) < q < 2\pi/(6\text{km})$ are not shown.
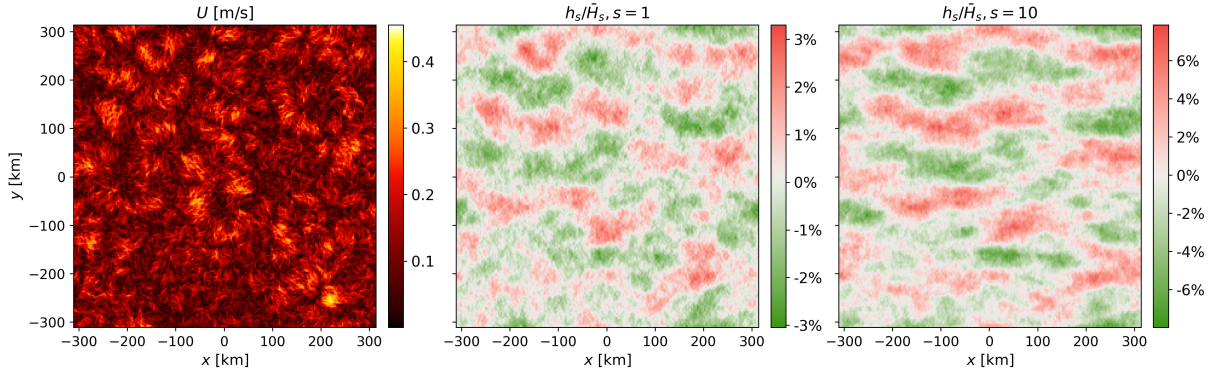

FIG. 7: SWH anomaly $h_s/\bar{H}_s$ (middle and right panels) induced by a current sample described in section 5. The left panel shows the current speed. The background waves follow the LHCS model described in appendix A, with directional-width parameter s taken to be 1 (middle panel) or 10 (right panel).

In figure 9, we show λ_x/λ_y as a function of the directionality s and for different values of the parameter α characterizing the relative importance of the divergent and rotational parts of the current. The other parameters are a described in section 4, with the spectral slope fixed as $\gamma = -3$. Except for purely divergent currents ($\alpha = 1$), λ_x/λ_y is greater than 1, reflecting elongation of the SWH patterns in the along-wave direction, and increasing with s for $s \gtrsim 1.5$.

For $s \gg 1$, $\lambda_x/\lambda_y \propto \sqrt{s}$, as is established by noting that

$$\left(\frac{\lambda_x}{\lambda_y}\right)^2 \propto \frac{\int \sin^2\varphi |\hat{L}_\psi(\varphi)|^2 \, d\varphi}{\int \cos^2\varphi |\hat{L}_\psi(\varphi)|^2 \, d\varphi} \propto s, \qquad (36)$$

since $\hat{L}_\psi \gg \hat{L}_\phi$ and $\hat{L}_\psi$ is localized within an $O(s^{-1/2})$ boundary layer around $\varphi = \pi/2$. This provides a scaling for the elongation of the streaks in h_s for highly directional waves.

For purely divergent currents ($\alpha = 1$), the aspect ratio is a constant (because $\hat{L}_\phi \propto \cos\varphi$), computed to be $\lambda_x/\lambda_y = 0.58 < 1$. This is why, in the rightmost $\alpha = 1.0$ panels of figures 1 and 2 (with $\alpha = 1$), h_s is somewhat elongated in the across-wave y-direction.

Along/across-wave spectra, $s = 1$

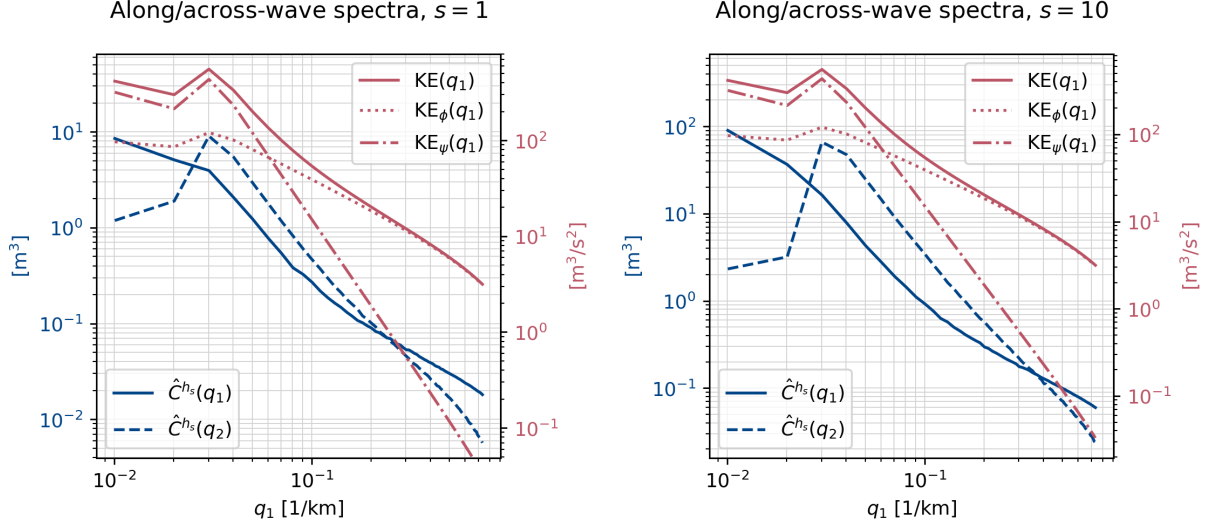

Along/across-wave spectra, $s = 10$

FIG. 8: Along/across-wave SWH spectra $\hat{C}^{h_s}(q_1)$ and $\hat{C}^{h_s}(q_2)$, and total, divergent and rotation KE spectra as functions of wavenumbers q_1 or q_2. The left vertical axis is for $\hat{C}^{h_s}(q_1)$ and the right vertical axis is for the KE spectra. The wave directional width parameter s is 1 (left panel) and 10 (right panel). Spectra outside $(200\text{km}) < q < 2\pi/(6\text{km})$ are not shown.
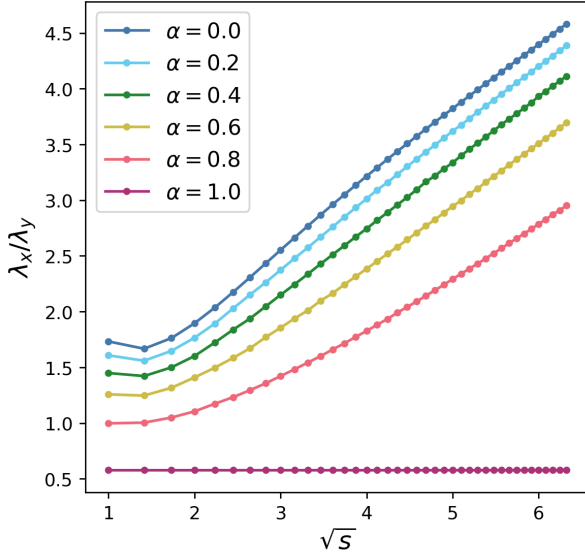

FIG. 9: Aspect ratio λ_x/λ_y of the SWH anomaly as a function of the directional-width parameter s and for different values of the parameters α controlling the ratio of rotational to divergent kinetic energy of the current.

7. Sensitivity to mean frequency

In preceding numerical examples we use mean radian frequency $\sigma_m = 0.61$ s^{-1}, corresponding to the mean pe-

riod $T_m = 10.3$ s. The background action spectrum $\bar{\mathcal{A}}(k, \theta)$ depends on σ_m (see appendix C) and the U2H functions $\hat{L}_\phi(\varphi)$ and $\hat{L}_\psi(\varphi)$ inherit this dependence through the integral

$$\int_0^\infty \bar{\mathcal{A}}(k, \theta) k^2 \mathrm{d}k \tag{37}$$

in (11). In this section, we examine the sensitivity of ℓ_ϕ and ℓ_ψ to σ_m.

In ocean-relevant situations, the dependence of ℓ_ϕ and ℓ_ψ on σ_m is comparable to the dependence on the directional spreading parameter s. This is inferred from figure 10 which shows ℓ_ϕ and ℓ_ψ as functions of both σ_m and s for wave spectra with fixed total energy, equivalently fixed $\bar{H}_s$. For oceanographic context, the leftmost panel of figure 10 shows an estimated probability density of σ_m and δ from 13 years (2010–2023) of wave buoy observations from Ocean Station Papa in the North Pacific Ocean. We chose Ocean Station Papa as a reference location due to its exposure to a broad range of wave conditions and its long history of meteorological and oceanographic observations (e.g., Large and Pond 1981; Thomson et al. 2013, and references therein). Directional wave buoy observations routinely provide the first four Fourier coefficients of the directional energy distribution, from which the mean frequency σ_m and mean directional spreading δ can be computed (Kuik et al. 1988). There are 195 580 samples included. To aid visualization, extreme observations with $\delta < 0.183$, $\delta > 1.118$, or $\sigma_m > 1.7$ s^{-1}, are deleted (0.5% of the data is discarded). The probability density plot indi-
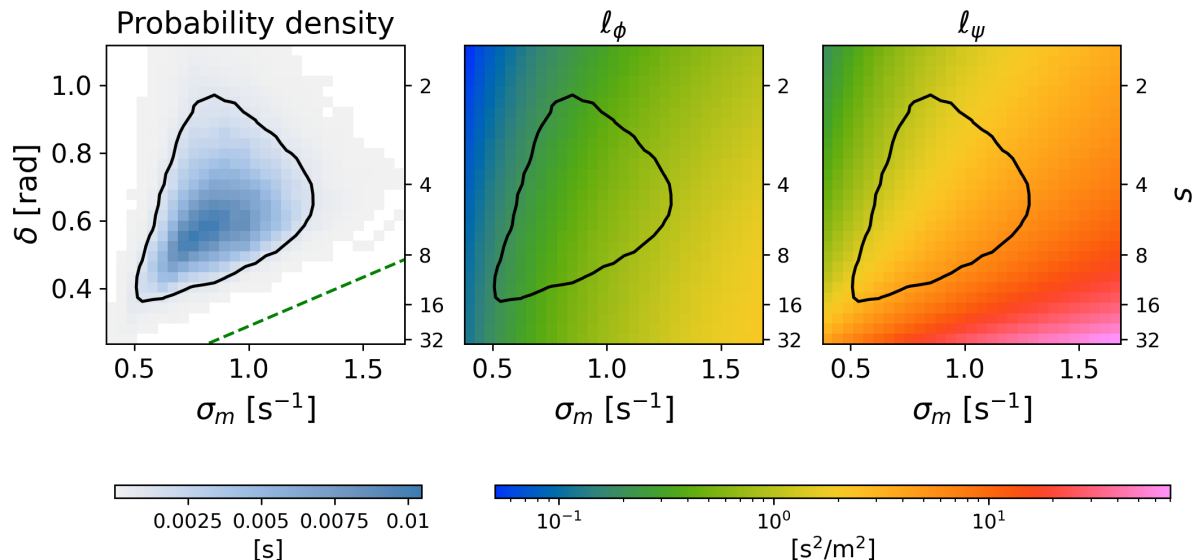
FIG. 10: Joint probability density of wave frequency σ_m and directional spreading δ from Ocean Station Papa observations (left panel) and U2H functions ℓ_ϕ (middle panel), and ℓ_ψ (right panel) as functions of (σ_m, δ), based on the LHCS model and the relation $\delta = (2/s)^{1/2}$. The probability density is constructed from 30×30 bins equally spaced in δ and σ_m with the color indicating the fraction of samples in each bin. The solid contour encloses bins with probability densities greater than 0.001 s; these bins enclose 92% of the data. Some values of s corresponding to δ are marked on the right vertical axes. The green dashed line in the left panel indicates the boundary of the linear regime (see (39) in Discussion).

cates the range of typical ocean values of δ and σ_m. As can be expected, short waves (large σ_m) are less directionally focused (larger δ) than long waves.

The second and third panels of figure 10 show ℓ_ϕ and ℓ_ψ computed by assuming the LHCS spectra for background waves, with directional spreading parameter $s = 2/\delta^2$. In summing the Fourier series (10), we cut n at ± 50, after verifying that $n = 100$ does not significantly change the results. For all relevant parameter values, $\ell_\phi \ll \ell_\psi$. ℓ_ϕ and ℓ_ψ in (25) increase with σ_m or, equivalently, with mean wavenumber $k_m = \sigma_m^2/g$, i.e. short high-frequency waves are more affected by currents and produce larger SWH anomalies than long low-frequency waves. The changes in ℓ_ψ produced by varying σ_m over the data range are comparable to those resulting from variations in s. For $s \gg 1$, in particular, we can show that $\ell_\psi \propto s^{3/2}\sigma_m^2$. The $s^{3/2}$ was noted in section 4; the σ_m^2 stems from the approximation

$$\int_0^\infty \bar{\mathcal{A}}(k,\theta)k^2 \mathrm{d}k \sim k_m^{1/2} \int_0^\infty \bar{\mathcal{A}}(k,\theta)k^{3/2}\mathrm{d}k$$
$$\sim k_m^{1/2}\bar{H}_s^2 \propto \sigma_m \bar{H}_s^2. \tag{38}$$

and the quadratic dependence of ℓ_ψ on the left-hand side (see (9)–(10) and (25)).

Earlier discussion emphasized the sensitivity of ℓ_ψ to changes in s. Here we emphasize that ℓ_ψ is equally sen-

sitive to changes in mean frequency σ_m. The same conclusion applies to the function $\hat{L}_\psi$ and hence to the SWH anomaly spectra.

8. Discussion

Key statistical features of current-induced SWH are explained by the U2H map which provides a linear relation between the anomalies of SWH and currents. U2H is deduced from the wave-action conservation equation by making a number of assumptions, chiefly the assumption (4) of current speeds small compared with wave group speeds. The physical effects captured by U2H identify the main mechanisms by which current induce SWH anomalies.

In U2H, advection of the action spectrum by currents is of secondary importance and is entirely neglected on the basis of $U/c_g \ll 1$. (See Ardhuin et al. (2017) for simulation results with and without advection.) Instead, currents affect the distribution of wave action, and hence of SWH, by inducing changes in both the direction and wavelength of SGWs (through refraction and the "concertina effect", respectively).

In U2H, refraction and concertina effects superpose linearly. It is straightforward to trace their contribution through the derivation of W25: refraction is associated with directional variations $\partial_\theta \bar{\mathcal{A}}$ of the background action and concertina effect with wavenumber variations $\partial_k \bar{\mathcal{A}}$.

Refraction can then be shown to contribute to the series in expression (10) for $\hat{L}_\psi$. The remaining term in $\hat{L}_\psi$ and the entirety of $\hat{L}_\phi$ are proportional to $\boldsymbol{P}$, which can be attributed to a combination of refraction and concertina effect, with respective weights $-1/2$ and $3/2$. For highly directional waves, $|\hat{L}_\psi| \gg |\hat{L}_\phi|$ and $\hat{L}_\psi$ is dominated by the series in (10), so we conclude that refraction, driven by vorticity, is the primary mechanism of current-induced SWH anomalies. This is consistent with the classical result showing that under asssumption (4) ray curvature is determined by vorticity (Landau and Lifshitz 2013; Kenyon 1971; Dysthe 2001; Gallet and Young 2014).

While this paper focuses on statistical predictions, we emphasize that U2H provides an approximation to the SWH anomaly induced by any specific current, as figures 1 and 2 illustrate. We also emphasize that the statistical assumptions we make (isotropy of the currents and, in some cases, independence of divergent and rotational currents) are not required by U2H. Rather, we make them to obtain simple, explicit predictions that explain generic features of wave–current interactions. The regime of highly directional waves is particularly robust to details of the current spectrum because the SWH anomaly is then controlled by the spectrum of the rotational current $\hat{C}^{U_\psi}(\boldsymbol{q})$ in a narrow wedge $\varphi \approx \pm\pi/2$ in $\boldsymbol{q}$-space and insensitive to both $\hat{C}^{U_\phi}(\boldsymbol{q})$ and $\hat{C}^{U_\phi U_\psi}(\boldsymbol{q})$

The validity of U2H depends on an assumption which has so far remained implicit. Because strong directionality, that is, large s, leads to strong SWH anomalies, a restriction is necessary to ensure that the linear approximation that underpins U2H applies. W25 discuss this and show that condition (4) needs tightening to

$$Us^{1/2}/c_g \ll 1. \tag{39}$$

We show the curve $Us^{1/2}/c_g = 1$ or equivalently, in terms of the directional spreading δ and mean frequency σ_m, $2\sqrt{2}U\sigma_m = g\delta$ for $U = 1$ m s^{-1} in the probability density plot in figure 10 (left panel). All data points are well above this green dashed line, indicating that the inequality (39) is satisfied. This suggests that (39) is only violated in rare circumstances, e.g. when current speeds are well in excess of 1 m s^{-1}.

Implicit to the linearity of U2H is the assumption that the wave spectrum deviates only little from a spatially uniform background. In reality, over large propagation distances, the scattering by currents has a cumulative impact that leads to the broadening of the SGW spectrum. Smit and Janssen (2019) and Villas Bôas and Young (2020) show that this broadening amounts to a directional diffusion of the action, ultimately leading to isotropic spectra (diffusion in frequency is weak as it depends on the time-dependence of the currents, see Cox et al. (2023)). The comparison between U2H and WW3 simulations in Villas Bôas et al.

(2020) suggests this directional diffusion is negligible over the scales of hundred of kilometers considered in this paper.

W25 note that, because the dependence of the SWH on both the divergent and rotational parts of the current, it is not in general possible to invert the U2H map and infer the current from SWH alone. It should however be possible to infer some useful statistical properties of the currents. For example, we show in section 6 that for highly directional waves, the across-wave KE spectra tend to have similar spectral slopes to the along/across-wave rotational KE within their spectral supports. Thus, if the assumptions involved are met, one can infer the slopes of rotational KE spectra from SWH spectra.

Data availability statement. Codes used for creating synthetic currents, computing the U2H map and plotting are accessible at https://github.com/hannnwang/U2H_examples.

APPENDIX A

Background wavenumber spectrum

The wavenumber dependence described by $f(k)$ in (13) is as in Wang et al. (2023). We detail its form to introduce the two parameters that appear, namely the mean frequency σ_m and the frequency spread δ_σ. We also show that the U2H map is insensitive to δ_σ.

We specify an SGW energy spectrum of the form $Z(\sigma)D(\theta)$ such that

$$\int_0^\infty \int_0^{2\pi} Z(\sigma)D(\theta)\,\mathrm{d}\sigma\,\mathrm{d}\theta = g\bar{H}_s^2/16. \tag{A1}$$

and choose a frequency dependence in the form of the truncated Gaussian

$$Z(\sigma) = \frac{g\bar{H}_s^2\, e^{-(\sigma-\sigma_m)^2/2\delta_\sigma^2}}{8\sqrt{2\pi}\delta_\sigma\,\mathrm{erfc}(-\sigma_m/\sqrt{2}\delta_\sigma)} \tag{A2}$$

with $\sigma > 0$, which introduces the two parameters σ_m and δ_σ.

The wavenumber dependence $f(k)$ in (1) is related to $Z(\sigma)$ via $Z(\sigma)\mathrm{d}\sigma = f(k)\sigma k\mathrm{d}k$ with $\sigma = \sqrt{gk}$. Therefore,

$$f(k) = \frac{g\bar{H}_s^2 \mathrm{e}^{-(\sigma(k)-\sigma_m)^2/2\delta_\sigma^2}}{8\sqrt{2\pi}\,\mathrm{erfc}(-\sigma_m/\sqrt{2}\delta_\sigma)\delta_\sigma\sigma(k)k}\frac{\mathrm{d}\sigma}{\mathrm{d}k}. \quad (A3)$$

The wavenumber dependence $f(k)$ affects the U2H map via the k-integral in (11). Using (A3), this integral is computed with help of a symbolic integrator:

$$\int_0^\infty f(k)k^2\,\mathrm{d}k = \frac{\bar{H}_s^2}{16}\sigma_m M\left(\frac{\delta_\sigma}{\sigma_m}\right), \quad (A4)$$

where

$$M(\tau) \overset{\text{def}}{=} 1 + \sqrt{\frac{2}{\pi}}\frac{\tau \mathrm{e}^{-\tau^{-2}/2}}{\mathrm{erfc}\left(-1/\sqrt{2}\tau\right)}. \quad (A5)$$

The function $M(\tau)$ increases with positive τ. For $0 < \tau < 0.5$, the value of M ranges in $(1, 1.028)$, which corresponds to a variation of less than 2.8%, an amount we regard as negligible. For higher τ, the function $M(\tau)$ increases faster: for $\tau = 1$, $M(1) = 1.29$, meaning that when δ_σ is as large as σ_m, the U2H map's operators can change by 29% in magnitude.

We assume δ_σ/σ_m is less than 0.5 and so neglect the impact of δ_σ on the U2H map. We set $\delta_\sigma = 0.04$ s^{-1}, which satisfies $\delta_\sigma/\sigma_m < 0.5$ for the range of σ_m considered here. With these values, the truncated Gaussian in (A2) is indistinguishable from a full Gaussian and σ_m and δ_σ are excellent approximations to the mean and standard deviations.

APPENDIX B

Cross-spectrum contribution

We show that provided that the cross-spectrum $\hat{C}^{U_\phi U_\psi}(q)$ is isotropic, it plays no role in the isotropic spectrum of the SWH anomaly and hence in the variances of the SWH and of its gradient. Therefore the results of sections 4 and 5 hold also for isotropic currents with correlated divergent and rotational components.

In the power spectral relation (20), integration of the cross-spectrum term in (20) with respect to φ leads to the term

$$2\,\mathrm{Re}\left(\hat{C}^{U_\phi U_\psi}(q)/q \int \hat{L}_\phi^*(\varphi)\hat{L}_\psi(\varphi)\,\mathrm{d}\varphi\right). \quad (B1)$$

which we now show vanishes.

The operator $\hat{L}_\phi(\varphi)$ in (9) can be written as

$$\hat{L}_\phi(\varphi) = -\frac{32}{g\bar{H}_s^2}\boldsymbol{P}\cdot\boldsymbol{e_q} = -\frac{32}{g\bar{H}_s^2}(P_1\cos\varphi + P_2\sin\varphi). \quad (B2)$$

Clearly then, only terms proportional to $\cos\varphi$ and $\sin\varphi$ in $\hat{L}_\psi^*(\varphi)$ can contribute to the integral (B1). Rearranging expression (10) for $\hat{L}_\psi(\varphi)$ as

$$\hat{L}_\psi(\varphi) = -\frac{64}{g\bar{H}_s^2}\boldsymbol{P}\cdot\boldsymbol{e_q^\perp} + \frac{16}{g\bar{H}_s^2}\sum_{|n|>1}n(-\mathrm{i})^{|n|}2\pi p_n \mathrm{e}^{\mathrm{i}n\varphi} \quad (B3)$$

isolates these term in $\boldsymbol{P}\cdot\boldsymbol{e_q^\perp}$. We then compute

$$\int \hat{L}_\phi(\varphi)\hat{L}_\psi^*(\varphi)\,\mathrm{d}\varphi \quad (B4)$$

$$= 2\left(\frac{32}{g\bar{H}_s^2}\right)^2 \int (\boldsymbol{P}\cdot\boldsymbol{e_q})(\boldsymbol{P}\cdot\boldsymbol{e_q^\perp})\,\mathrm{d}\varphi$$

$$= 2\left(\frac{32}{g\bar{H}_s^2}\right)^2 \left(\int P_1 P_2\cos^2\varphi\,\mathrm{d}\varphi - \int P_1 P_2\sin^2\varphi\,\mathrm{d}\varphi\right) = 0 \quad (B5)$$

using that $\boldsymbol{P}$ is real.

APPENDIX C

Numerical details of synthetic currents

For the synthetic currents in section 4, we draw current samples on square, 2500 km-wide grids with grid spacing of 2.5 km. For $2\pi/(200\text{km}) < q < 2\pi/(6\text{km})$, the isotropic spectra $K_\phi(q)$ and $K_\psi(q)$ follow the power laws q^γ. For larger wavenumbers, the spectra are set to decay rapidly. For smaller wavenumbers, they are set as zero in order to alleviate artifacts from a square, non-isotropic spectral grid. The currents are drawn so that the Fourier coefficients of the potential and streamfunction follow zero-mean, random phase distributions, independent at each wavenumber except when the reality condition demands. The potential and streamfunction are independent.

The synthetic currents shown in figures 1 and 2 are drawn similarly. The only difference is that for sake of demonstration, we draw a single random function, $\hat{\Phi}$ say, and take the streamfunction and potential as $\hat{\psi} = \sqrt{\alpha}\,\hat{\Phi}$ and $\hat{\phi} = \sqrt{1-\alpha}\,\hat{\Phi}$ so that they are correlated. This choice is made in order that the current speeds remain unchanged in each row, despite different α in figures 1 and 2.

References

Ardhuin, F., S. T. Gille, D. Menemenlis, C. B. Rocha, N. Rascle, B. Chapron, J. Gula, and J. Molemaker, 2017: Small-scale open ocean currents have large effects on wind wave heights. *Journal of Geophysical Research: Oceans*, **122 (6)**, 4500–4517.

Balwada, D., J. H. LaCasce, and K. G. Speer, 2016: Scale-dependent distribution of kinetic energy from surface drifters in the gulf of mexico. *Geophysical Research Letters*, **43 (20)**, 10–856.

Bühler, O., J. Callies, and R. Ferrari, 2014: Wave–vortex decomposition of one-dimensional ship-track data. *Journal of Fluid Mechanics*, **756**, 1007–1026.

Cavaleri, L., B. Fox-Kemper, and M. Hemer, 2012: Wind waves in the coupled climate system. *Bulletin of the American Meteorological Society*, **93 (11)**, 1651–1661.

Chereskin, T. K., C. B. Rocha, S. T. Gille, D. Menemenlis, and M. Passaro, 2019: Characterizing the transition from balanced to unbalanced motions in the southern california current. *Journal of Geophysical Research: Oceans*, **124 (3)**, 2088–2109.

Cox, M. R., H. A. Kafiabad, and J. Vanneste, 2023: Inertia-gravity-wave diffusion by geostrophic turbulence: the impact of flow time dependence. *Journal of Fluid Mechanics*, **958**, A21.

Dysthe, K., 2001: Refraction of gravity waves by weak current gradients. *Journal of Fluid Mechanics*, **442**, 157–159.

Edson, J. B., and Coauthors, 2013: On the exchange of momentum over the open ocean. *Journal of Physical Oceanography*, **43 (8)**, 1589–1610.

Gallet, B., and W. R. Young, 2014: Refraction of swell by surface currents. *Journal of Marine Research*, **72 (2)**, 105–126.

Kenyon, K. E., 1971: Wave refraction in ocean currents. *Deep-Sea Research*, **18**, 1023–1034.

Kuik, A., G. P. Van Vledder, and L. Holthuijsen, 1988: A method for the routine analysis of pitch-and-roll buoy wave data. *Journal of Physical Oceanography*, **18 (7)**, 1020–1034.

Landau, L. D., and E. M. Lifshitz, 2013: *Fluid Mechanics: Course of Theoretical Physics, Volume 6*. Elsevier.

Large, W., and S. Pond, 1981: Open ocean momentum flux measurements in moderate to strong winds. *Journal of physical oceanography*, **11 (3)**, 324–336.

Lenain, L., and N. Pizzo, 2021: Modulation of surface gravity waves by internal waves. *Journal of Physical Oceanography*, **51 (9)**, 2735–2748.

Longuet-Higgins, M. S., D. E. Cartwright, and N. Smith, 1963: Observations of the directional spectrum of sea waves using the motions of a floating buoy. *Ocean Wave Spectra*, S. EC, Ed., Prentice-Hall, Englewood Cliffs, New Jersey, 111–136.

Phillips, O. M., 1977: *The Dynamics of the Upper Ocean*. Cambridge University Press.

Quilfen, Y., and B. Chapron, 2019: Ocean surface wave-current signatures from satellite altimeter measurements. *Geophys. Res. Lett.*, **46 (1)**, 253–261.

Rascle, N., B. Chapron, A. Ponte, F. Ardhuin, and P. Klein, 2014: Surface roughness imaging of currents shows divergence and strain in the wind direction. *Journal of Physical Oceanography*, **44 (8)**, 2153–2163.

Rascle, N., F. Nouguier, B. Chapron, A. Mouche, and A. Ponte, 2016: Surface roughness changes by finescale current gradients: Properties at multiple azimuth view angles. *Journal of Physical Oceanography*, **46 (12)**, 3681–3694.

Rocha, C., T. Chereskin, S. Gille, and D. Menemenlis, 2016: Mesoscale to submesoscale wavenumber spectra in Drake Passage. *Journal of Physical Oceanography*, **46 (2)**, 601–620.

Romero, L., D. Hypolite, and J. C. McWilliams, 2020: Submesoscale current effects on surface waves. *Ocean Modelling*, 101662.

Romero, L., L. Lenain, and W. K. Melville, 2017: Observations of surface wave–current interaction. *Journal of Physical Oceanography*, **47 (3)**, 615–632.

Smit, P. B., and T. T. Janssen, 2019: Swell propagation through sub-mesoscale turbulence. *Journal of Physical Oceanography*, **49 (10)**, 2615–2630.

Taylor, P. K., and M. J. Yelland, 2001: The dependence of sea surface roughness on the height and steepness of the waves. *Journal of physical oceanography*, **31 (2)**, 572–590.

Thomson, J., E. D'Asaro, M. Cronin, W. Rogers, R. Harcourt, and A. Shcherbina, 2013: Waves and the equilibrium range at ocean weather station p. *Journal of Geophysical Research: Oceans*, **118 (11)**, 5951–5962.

Tolman, H. L., and Coauthors, 2009: User manual and system documentation of WAVEWATCH III version 3.14. *Technical note, MMAB Contribution*, **276**, 220.

Villas Bôas, A. B., B. D. Cornuelle, M. R. Mazloff, S. T. Gille, and F. Ardhuin, 2020: Wave–current interactions at meso-and submesoscales: Insights from idealized numerical simulations. *Journal of Physical Oceanography*, **50 (12)**, 3483–3500.

Villas Bôas, A. B., and W. R. Young, 2020: Directional diffusion of surface gravity wave action by ocean macroturbulence. *Journal of Fluid Mechanics*, **890**, R3.

Wang, H., A. B. Villas Boâs, J. Vanneste, and W. R. Young, 2025: Scattering of surface waves by ocean currents: the U2H map. *J. Fluid Mech.*, **1005**, A12.

Wang, H., A. B. Villas Boâs, W. R. Young, and J. Vanneste, 2023: Scattering of swell by currents. *J. Fluid Mech.*, **975**, A1.